Journal of Materials Chemistry A

Accepted Manuscript

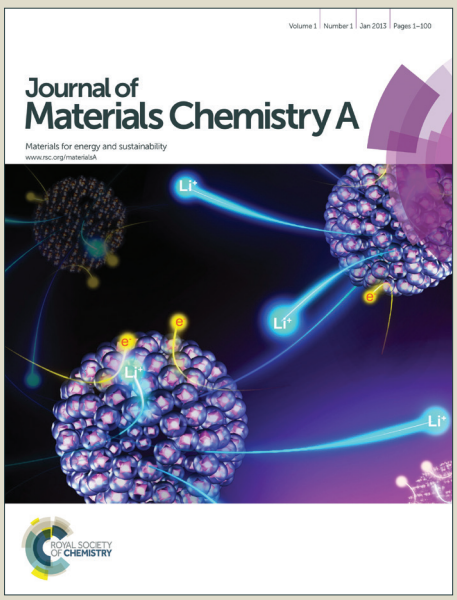

ROYAL SOCIETY OF CHEMISTRY

www.rsc.org/materialsA

Low temperature combustion synthesis of nitrogen-doped graphene for metal-free catalytic oxidation

Stacey Indrawirawan, Hongqi Sun*, Xiaoguang Duan, Shaobin Wang*

Department of Chemical Engineering, Curtin University, GPO Box U1987, Perth, WA 6845, Australia

*Correspondence Authors.

Email: shaobin.wang@curtin.edu.au (S. Wang), h.sun@curtin.edu.au (H. Sun)

Graphical Abstract

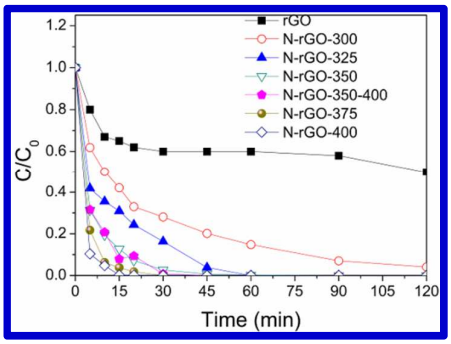

A mild synthesis method was developed to improve metal-free catalysis of graphene in catalytic oxidation by nitrogen modification, which can be easily tailored by varying calcination temperature.

Abstract

Nitrogen-doped reduced graphene oxide (N-rGO) was prepared by a simple process of simultaneous reduction and nitrogen doping on graphene oxide (GO) at low temperatures using ammonium nitrate as a N precursor. Characterization techniques indicated that N-rGO materials with high N loading (5-8 at.%) can be easily produced and that the crystal-/micro-structures and chemical compositions of N-rGO materials are dependent on the calcination conditions. The metal-free catalysis of N-rGO was investigated in catalytic activation of peroxymonosulfate (PMS) for phenol oxidative degradation in water. It was found that N-rGO samples are promising green catalysts for phenol degradation. Kinetic studies showed that phenol degradation follows first order reaction kinetics on N-rGO-350 with activation energy of 31.6 kJ/mol. The mechanism of PMS activation and phenol oxidation was elucidated by employing both electron paramagnetic resonance (EPR) studies and quenching tests with ethanol and tert-butanol.

Keywords: nitrogen doping; graphene; peroxymonosulfate; phenol degradation; metal-free

1. Introduction

One of the most critical issues in industrialization is the discharge of polluted water that largely contains particles, organics, and heavy metal ions.[1] Many water treatment technologies have been established, such as adsorption, filtration, evaporation, and membrane separation, to remediate the organic contaminations. [2] Advanced oxidation processes (AOPs) using metal-based materials as catalysts have attracted more attention over those physical processes due to the complete decomposition of organic pollutants. [3, 4]

As an excellent alternative to hydroxyl radicals (•OH), sulfate radicals (SO_4•$^-$) have been widely applied to decompose organic pollutants. [5-8] However, metal-based catalysts, such as cobalt and manganese oxides, are expensive and sometimes toxic metal leaching in either homogeneous or heterogeneous catalysis can lead to secondary contamination.[4, 6, 7] Therefore, metal-free green catalysts are highly recommended for environmental remediation. [9]

Graphene is a single sheet of graphite and has impressive theoretical surface area of 2630 m^2/g, chemical stability, open porous structure, and high electrical conductivity.[10, 11] Therefore, it can be a promising candidate of green catalysts. In a previous study, reduced graphene oxide (rGO) was firstly discovered to be effective for activation of peroxymonosulfate (PMS) to produce sulfate radicals. The catalytic activity of rGO can be improved by increased porosity and specific surface area (SSA) and manipulated surface functional groups. [10, 12, 13] Structural modification was conducted by CO_2 activation to obtain highly porous rGO (A-rGO-25, A-rGO-60 and A-rGO-75). It was found that 100% methylene blue (MB) removal would be achieved in 4 h for rGO, and that the same efficiency would be obtained in 1.5 h on A-rGO-25 after CO_2 activation, 1.0 h on A-rGO-60 and 2 h on A-rGO-75. [10] Physical and chemical activation of rGO using different reagents, CO_2, $ZnCl_2$ and CO_2/$ZnCl_2$, were further carried out to obtain highly porous metal-free carbonaceous materials for adsorption and catalytic oxidation. The study showed that specific surface area and oxygen containing groups are two important factors determining the adsorptive and catalytic performances. [12]

It was also reported that the performances of graphene can be improved by doping with other elements such as nitrogen, boron, halogen, sulphur or metals.[13-18] Qu et al.[19] reported that nitrogen-doped graphene can show much better electrocatalytic activity for oxygen reduction

in fuel cells than platinum. The superior catalytic activity of nitrogen-doped graphene was also demonstrated in aerobic selective oxidation of benzylic alcohols, and the graphitic nitrogen was suggested to be the active sites.[20] Gao et al.[21] examined the catalytic performances of nitrogen doped graphene and concluded that graphitic nitrogen is effective for activation of C-H bonds in selective oxidation by changing the electronic structure of sp^2 carbon atoms. A recent study has discovered that nitrogen doped reduced graphene oxide (N-rGO) showed an enhanced activity for aqueous organic oxidation by activation of peroxymonosulfate (PMS or oxone) in phenol solution. [17] The performance of this N-rGO as a green catalyst has been studied under the thermal annealing temperature at 350 °C. Such a condition was also found to be effective for nitrogen modification of carbon nanotubes, which were able to activate both PMS and PDS (persulfate). [22] In this study, we report further investigation on the effect of the thermal annealing temperature on the physicochemical properties of N-rGO and their performances in aqueous oxidation of phenol solutions.

2. Experimental

2.1 Materials and chemicals

Graphite powder, sulphuric acid (95-97%), ammonium nitrate, acetonitrile and potassium peroxymonosulfate (Oxone®) were obtained from Sigma-Aldrich. Hydrogen peroxide (30%), ethanol, methanol and hydrochloric acid (32%) were obtained from Chem-Supply. Potassium permanganate and phenol were obtained from Ajax Finechem.

2.2 Synthesis of graphene oxide (GO)

Synthesis of graphene oxide (GO) was carried out using a modified Hummers' method. [23] In a typical synthesis, graphite powder was mixed with a strong oxidizer of concentrated H_2SO_4 and then $KMnO_4$ was slowly added. The mixture was stirred at 35 °C for 5 h. Deionized (DI) water was then slowly added into the mixed solution and the temperature was kept carefully below 98 °C. The suspension was then treated by H_2O_2 to reduce the residual permanganate. The obtained GO slurry was separated by centrifugation and washed using HCl and DI water three times. The final product was ground after drying in an oven at 60 °C for at least 48 h.

2.3 Preparation of nitrogen-doped reduced graphene oxide (N-rGO)

The reduction process and nitrogen doping were conducted simultaneously using ammonium nitrate as the N precursor. [17] GO and ammonium nitrate at 1.0 g each were mixed in 50 mL

ethanol at room temperature for 30 min, then the temperature was increased to 50 ℃ and stirred for a few hours until the ethanol was completely evaporated. The dried mixture was thermally annealed at different temperatures in the range of 300 to 400 °C for 1 h. The N-rGO was obtained after being washed using ethanol and DI water three times, and drying in the oven at 60 °C. The obtained samples were denoted as N-rGO-n and n is referring to the annealing temperature. In addition, further thermal annealing of N-rGO-350 was carried out by employing nitrogen gas atmosphere at 400 °C for 1 h to obtain another sample, N-rGO-350-400.

2.4 Characterization of nitrogen doped reduced graphene oxide

X-ray diffraction (XRD) patterns were acquired on a Bruker D8-Advanced X-ray instrument using Cu-Kα radiation with λ at 1.5418 Å. Nitrogen sorption isotherms were obtained using a Tristar II 3020 after degassing the samples at 110 ℃ for 4 h. The Brunauer-Emmett-Teller (BET) equation and Barrett-Joyner-Halenda (BJH) method were utilized to evaluate the specific surface area, and pore size distribution of the samples, respectively. Fourier transform infrared spectra (FTIR) were obtained from a Bruker instrument with ATR correction mode. X-ray photoelectron spectroscopy (XPS) was carried out to determine the chemical states of elements using a Thermo Escalab 250 with Al-Kα X-ray. Thermogravimetric-differential thermal analysis (TG-DTA) was carried out by heating the samples in an air flow at a rate of 100 mL/min using a Perkin-Elmer Diamond TGA/DTA thermal analyzer with a heating rate of 10 °C/min. Scanning electron microscopy (SEM) was applied to investigate the morphology of the catalysts on Zeiss Neon 40 EsB FIBSEM. Raman analysis was performed on an ISA dispersive Raman spectrometer using argon ion lasers (514 nm). Electron paramagnetic resonance (EPR) spectra were obtained on a Bruker EMS-plus to detect the free radicals generated during activation of PMS.

2.5 Catalytic oxidation of phenol solutions

The catalytic oxidation of phenol was carried out in a 500 mL conical flask with phenol solution (20 ppm), catalyst (0.2 g/L) and PMS (2.0 g/L) in a constant-temperature controlled water bath for the kinetic studies. At each time interval, 1 mL solution was withdrawn by a syringe, filtered by a 0.45 μm Millipore film, and injected into a vial. Then 0.5 mL of methanol as a quenching reagent was also injected into the reaction solution. The mixed

solution was analyzed by a high performance liquid chromatography (HPLC, Varian) with a C-18 column and a UV detector set at 270 nm.

3. Results and Discussion

3.1 Characterization of materials

After oxidization of graphite by the modified Hummers' method, [23] the peak in XRD pattern at 2θ = 9.9° (002 plane) clearly indicated the formation of graphene oxide (GO) from the oxidation of graphite (Fig. S1a), which has a typical peak at around 2θ = 26°. Fig. 1 shows XRD patterns of N-rGO samples. The peak at 2θ = 9.9° (002 plane) disappeared and a new peak at 2θ = 25.5° (corresponding to the interplanar spacing of 0.35 nm) was observed on all N-doped samples. The changes in XRD patterns suggested the successful reduction of GO to rGO along with nitrogen doping process. [24]

In general, graphene has three types of ordered crystal structures dependent on the stacking sequences of graphene sheets. These three different stacking sequences are simple hexagonal (AAA), hexagonal (Bernal stacking, ABAB) and rhombohedral (ABC).[25] For graphene with hexagonal AB and ABC stacking, the interlayer spacing is 0.335 and 0.337 nm, respectively.[26] In this study, the interlayer spacing of N-rGO was about 0.35 nm. The interplanar spacing of N-rGO was slightly larger than that of graphite (0.34 nm) for (002) plane due to the presence of oxygen functional groups and water molecules. [27] The peak (2θ = 25.5°) broadening might be attributed to the large strain in the lattice induced by the presence of hydroxyl and epoxide groups on both sides of rGO layers.[28] The large strain is related to the distortion of lattice periodicity of the carbon-carbon distance. Further annealing N-rGO-350 in N_2 at 400 ^oC would decrease the intensity of the characteristic peak at around 2θ =25.5°, as shown in Fig. S1b.

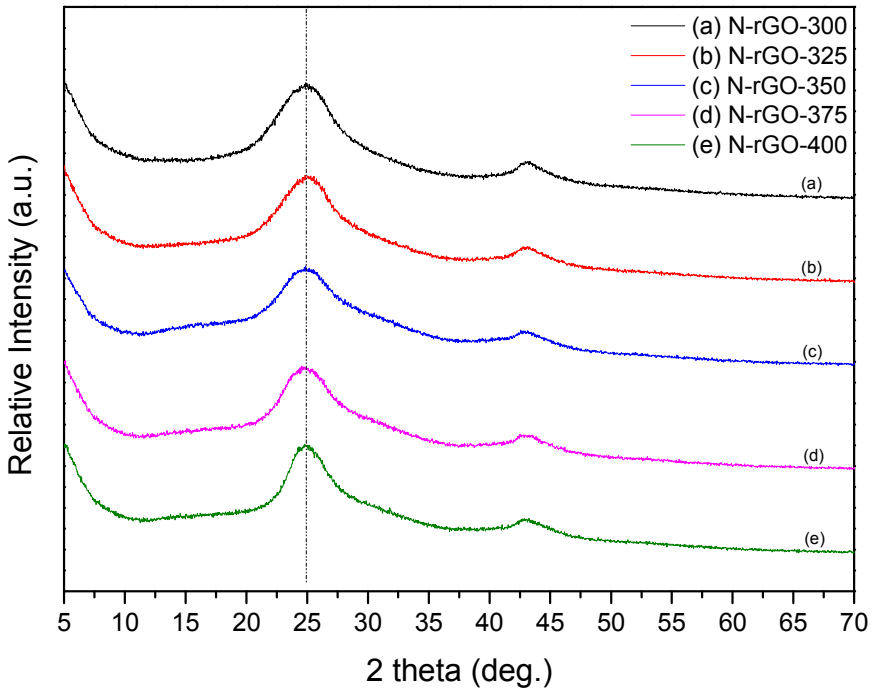

Figure 1 XRD patterns of N-rGO via different thermal annealing temperatures.

The detailed information of crystal structures of N-rGO samples are shown in Table 1. Peak broadening at different thermal annealing temperatures can be compared by the half peak width (HPW, B). Thermal treatment and associated reduction process would reduce the HPW compared to that of GO. Moreover, HPW decreased with the increased temperature. Also, HPW of N-rGO-350-400 (3.4 ^{o}) was much narrower than that N-rGO-35 (5.6 ^{o}). The changes of HPW values indicated the degree of reduction, removal of oxygen functional groups, and distortion of the lattice periodicity. The origin of the B changes may be due to the increase of the interlayer thickness, L,[29] as shown in Table 1.

Table 1 Crystal- and micro-structures of N-rGO samples.

Sample	Half peak width (B, ^{o})	Interlayer material thickness (L, nm)	D band (cm^{-1})	G band (cm^{-1})	I_D/I_G ratio	SSA (m^2/g)
N-rGO-300	5.8	3.12	1323	1589	1.32	53
N-rGO-325	5.6	3.23	1323	1580	1.40	58
N-rGO-350	5.6	3.23	1323	1577	1.26	99
N-rGO-350-400	3.4	5.33	1335	1583	1.21	91
N-rGO-375	5.1	3.55	1329	1586	1.38	127
N-rGO-400	4.4	4.11	1329	1580	1.41	159

Fig.2 shows Raman spectra of GO and N-rGO prepared at different thermal annealing temperatures. The G bands (originated from in-plane vibrations of sp^2 carbon in rGO domains) appear at about 1580 cm^{-1} and strong D bands (related to the edges, defects, and structurally disordered carbon) occur at about 1320 cm^{-1}. These results are consistent with previous Raman investigations on GO. [30-32] The I_D/I_G ratio (intensity ratio of D band to G band) of the GO was 1.18, and those ratios of N-rGO via different thermal annealing temperatures are tabulated in Table 1. The I_D/I_G ratio shows the degree of defects in rGO materials. [24]

As seen in Table 1, the I_D/I_G ratios of N-rGO via different calcination conditions significantly increased after the thermal annealing, compared with that of GO. The increased I_D/I_G ratio by thermal annealing indicates the enhanced defective edges, and declined sp^2 carbon of rGO structure. [32] However, among the N-rGO samples, no temperature dependent I_D/I_G ratio was observed, indicating the complicated processes of simultaneous reduction and nitrogen doping, as nitrogen doping might be able to adjust the defective structure as well.

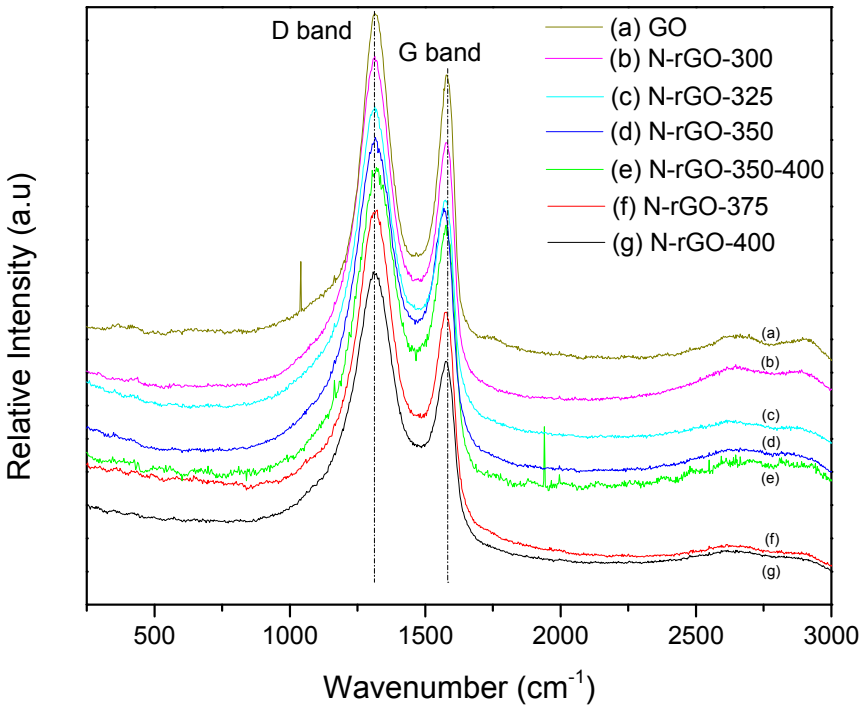

Figure 2 Raman spectra of GO and N-rGO samples.

The morphologies of GO, N-rGO-300 and N-rGO-400 were observed by SEM imaging. As shown in Fig. 3(a) GO had a wrinkled and sponge-like structure due to the exfoliation and restacking process. For N-rGO-300 and -400 (Fig. 3(b) and 3(c)), SEM micrographs show irregularly enfolding and layered structures tangled with each other due to the exfoliation. These results confirm that thermal annealing was able to exfoliate the stacked layers of GO, and improve the microstructure, resulting in a higher specific surface area (SSA) as shown in Table 1.

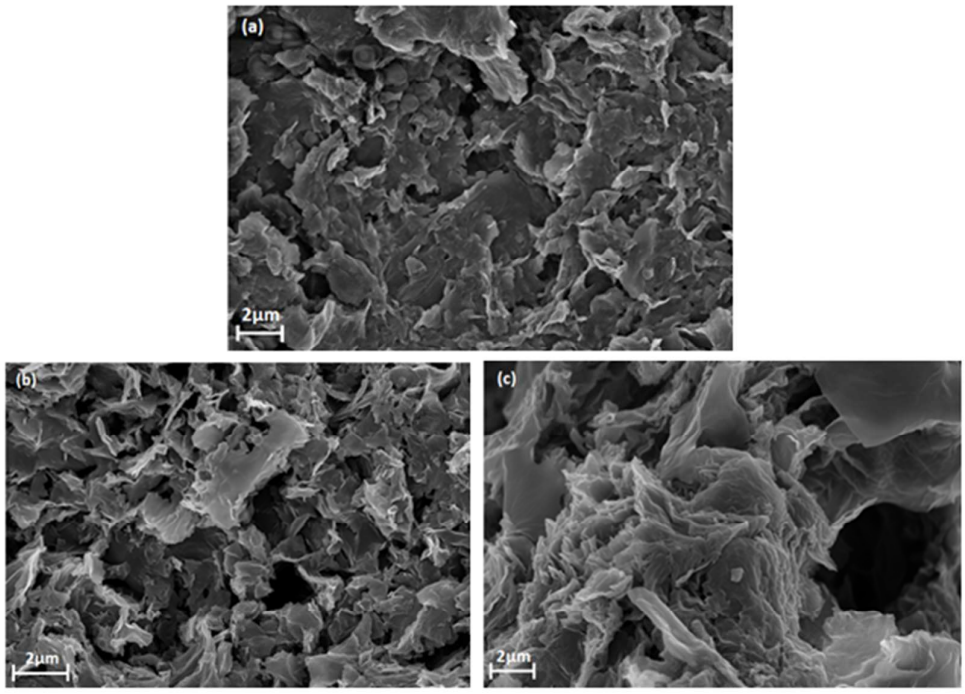

Figure 3 SEM images of (a) GO, (b) N-rGO-300 and (c) N-rGO-400

In atomic scope of the structures of GO and rGO, both sides of the basal plane have randomly intermixed oxygen groups, such as hydroxyl and epoxide groups[33, 34]. Meanwhile, carbonyl and carboxylic groups are attached at the sheet edges. It was reported that decompositions of the hydroxyl and epoxy sites would occur in thermal treatment and result in a build-up of pressure between adjacent graphene oxide sheets.[35] Therefore, thermal exfoliation may occur when the pressure exceeds the Van der Waals interlayer attraction.

The textural information of N-rGO samples were investigated by N_2 sorption isotherms, as shown in Fig. 4. The SSA values of N-rGO samples prepared at different temperatures are tabulated in Table 1. In general, nitrogen doping and thermal treatment at 300 - 400 °C imposed a significant effect on SSA values. Surface area increased with increasing calcination temperature. At 350 °C, a rather significant exfoliation occurred as indicated by the increased SSA value from about 58 to 99 m^2/g. At the thermal annealing temperatures of 375 and 400 °C, the SSA values are 127 and 159 m^2/g, respectively. While further annealing the sample of N-rGO-350 at 400 °C in nitrogen would slightly decrease the SSA of N-rGO-350-400.

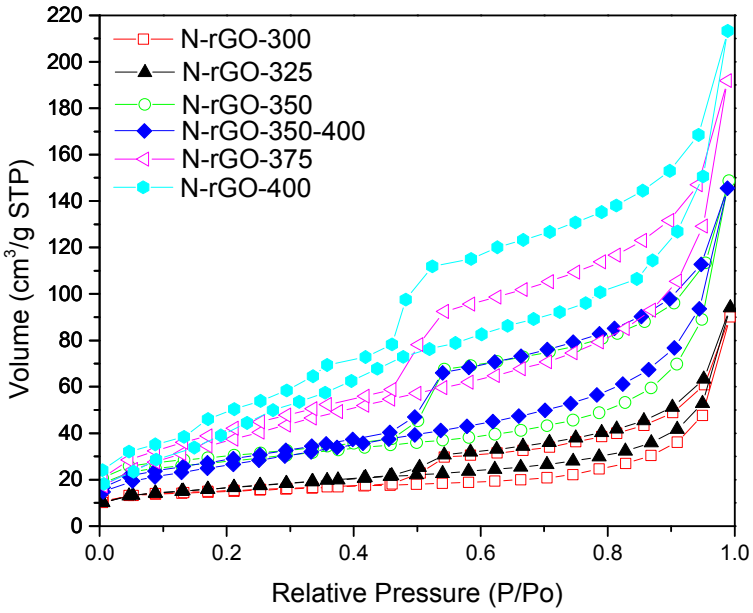

Figure 4 N_2 sorption isotherms of N-rGO samples.

The thermal behaviors of GO and N-rGO-400 were investigated by TGA-DTA. The curves of GO and N-rGO-400 are presented in Fig. 5(a) and (b), respectively. The analysis was performed in air at a heating rate of 10 °C/min. Fig. 5(a) shows that the weight loss of GO occurs from starting temperature to 100 °C primarily due to the evaporation of thermally unstable water molecules. [36, 37] Further weight loss was observed from 100 up to 450 °C due to the removal of the oxygen functional groups. [35, 38, 39] It was also found that from 100 to 450 °C, the DTA curve shows a characteristic step or peak at 180 °C. From 450 to 540 °C, the DTA curve also shows a characteristic step or peak at 520 °C corresponding to the thermal decomposition of carbon structure. These two peaks are corresponding to the strong exothermal peaks and in good agreement with previous studies. [37] There was no further weight loss of GO after reaching the temperature of 540 °C. Fig. 5(b) indicates that there are three regions on N-rGO-400 weight loss process. First, a minor weigh loss occurs from room temperature to about 110 °C which may be due to the evaporation of adsorbed water molecules. Second, another minor weight loss occurs from 110 to 450 °C attributed to the removal of residue oxygenated functional groups generating CO_2 and H_2O. [35, 38, 39] Finally, a

major weight loss can be observed between 450 and 550 °C. The TGA and DTA curves show a characteristic step or strong exothermal peak at 530 °C due to the carbon combustion and decomposition. [11, 39] No further weight loss of N-rGO-400 can be observed after 550 °C. In this study, the weight losses of N-rGO-400 and GO before 450 °C are about 5% and 54%, respectively. These results suggested that a substantial amount of water and oxygen functional groups were removed by simultaneous process of reduction and nitrogen doping using ammonium nitrate as N precursor.

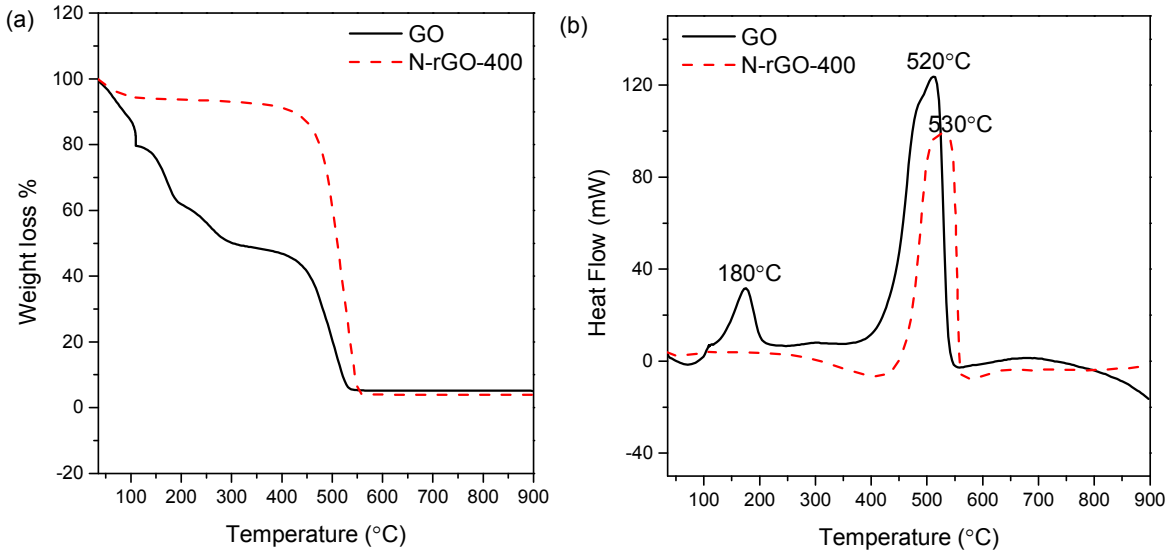

Figure 5 (a) TGA and (b) DTA curves of GO and N-rGO-400 in air atmosphere.

Fig. 6 displays FTIR spectra of N-rGO samples. The spectrum of GO displays several characteristic peaks, such as O-H group (hydroxyl) at 3323 cm^{-1} , C=O group (carbonyl) at 1715 cm^{-1}, C=C group (aromatic) at 1586 cm^{-1} and C-O group (epoxy or alkoxy) at 1035 cm^{-1}. These results are consistent with reported values. [12, 40, 41] Compared to GO, the signals of oxygen functional groups of N-rGO are very weak indicating the presence of less oxygen groups attached to the surface. For N-rGO, the absorption bands at approximate 1560 and 1200 cm^{-1} are attributed to the C=C/C=N groups and C-N groups, respectively [42].

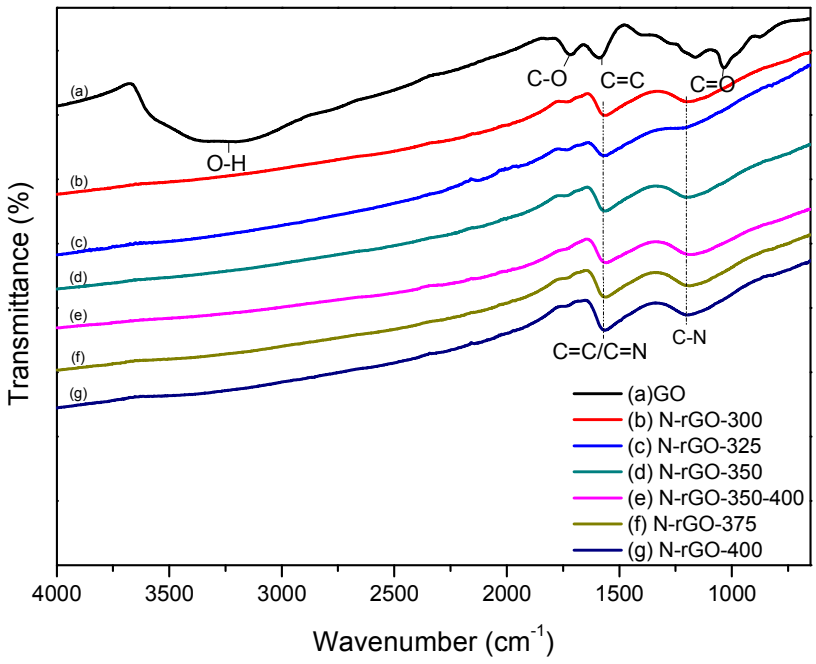

Figure 6 FTIR spectra of GO and N-rGO materials.

Fig. 7 shows XPS studies of the different N-rGO samples. The XPS analysis was carried out to investigate atomic concentration (at.%) of nitrogen contents in N-rGO via different calcination temperatures. The O/C (oxygen versus carbon) and N/C (nitrogen versus carbon) ratios are tabulated in Table 2.

Table 2 Chemical compositions of various N-rGO materials.

Sample	N level, at. %	N/C ratio	Pyridinic N, at. %	Pyrrolic N, at. %	Graphitic N, at. %	O/C ratio
N-rGO-300	5.8	0.078	1.9	3.1	0.8	0.28
N-rGO-325	7.2	0.085	2.4	4.2	0.6	0.11
N-rGO-350	6.4	0.075	2.2	3.7	0.5	0.10
N-rGO-375	7.0	0.081	2.5	3.8	0.7	0.08
N-rGO-400	6.7	0.079	2.3	3.5	0.9	0.10

Fig. 7(a) shows XPS surveys of the N-doped rGO samples prepared at different temperatures. The corresponding C 1s, O 1s and N 1s peaks are centred at 284.6, 531, and 399.5 eV, respectively.[43-45] Based on the compositional information of carbon, oxygen and nitrogen, it can be found that treatment temperature has varying effect on the nitrogen and oxygen levels of the samples. High resolution of XPS N 1s spectra of N-rGO can be found in Fig. 7(b). Three types of nitrogen species can be identified from the de-convolution of XPS N 1s spectra: pyridinic (N-6) at 398.3 eV, pyrrolic (N-5) at 399.8 eV, and graphitic N at 401.8 eV [45-49]. Table 2 shows that the contents of pyridinic N, pyrrolic N, and graphitic N vary from 1.5%-2.5%, 3%-4.5%, and 0-1%, respectively. For all the N-rGO samples, the content of pyrrolic N was generally higher than the pyridinic N and graphitic N. Fig. S2 shows the de-convolution C1s XPS spectra of N-rGO samples. A broad C 1s peak indicated five different C species in the range of 281 - 291 eV. For N-rGO-400, the C-C bond, C-N bond, C=N bond, C=O bond, and O-C=O bond occur at 284.6, 285.8, 286.8, 288, and 290.5 eV, respectively. [24, 50-53]

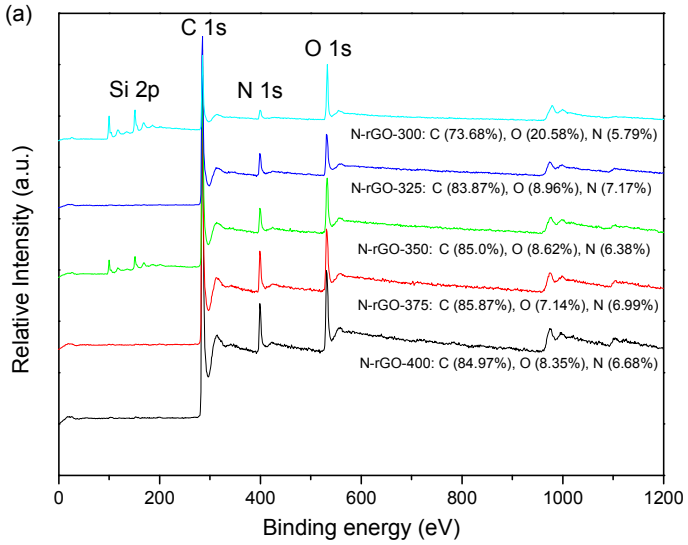

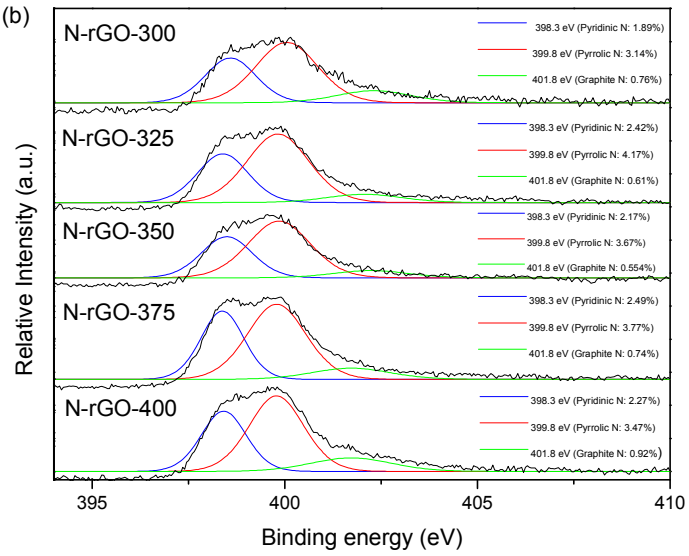

Figure 7 (a) XPS survey and (b) N 1s of N-rGO samples.

Previous studies showed that N-doping can occur at temperature as low as 80 °C and up to 1100 °C for reduced graphene oxide by thermal or hydrothermal treatment of GO with ammonia or urea or hydrazine and that ammonia can produce the highest nitrogen doping level at 500 °C.[43, 49, 54] The nitrogen doping level will decrease significantly when the temperature is above 500 °C. Thermal treatment at 900 °C and above would result in breaking up of C-N bonds and removing off of the nitrogen from N-rGO. In general, the nitrogen atoms will be assigned to pyridinic-N, pyrrolic-N and graphitic-N forms. At low calcination temperatures, the C-N bond formations occur predominantly on the defect sites (zigzag or armchair) in the plane, where the C atoms are more chemically reactive than those in the perfect lattice. The concentration of graphitic N was found to increase with increasing annealing temperature, whereas the concentration of pyridinic-N will decrease with increasing annealing temperature.[20, 43, 45] In a recent study, for the mixture of GO and ammonium nitrate annealed at 350 °C, the N-rGO contains 5.61 at.% nitrogen with the compositional nitrogen ratio of graphitic: pyridinic: pyrrolic at 1: 1.46 : 2.45.[17] For GO, carbocyclic and lactone groups begin to decompose at about 250 °C, whereas carbonyl and -COOH groups are decomposed at about 450 °C. Therefore, it is suggested that these oxygen functional groups in the GO are mostly responsible for reaction with ammonia to form C-N bonds.[43] In this study, the mixture of ammonium nitrate and GO was thermally annealed between 300-400 °C to produce nitrogen doped rGO. The temperature was high enough for

the decomposition of certain oxygen functional groups with ammonium nitrate to form the C-N bonds. As seen in Table 2, it appeared that no direct correlation between the nitrogen doping level and the temperature could be derived.

3.2 Catalytic oxidation of phenol

The effect of calcination temperature on the performance of catalytic phenol oxidation on rGO and various N-rGO is shown in Fig. 8. For rGO without nitrogen doping, 50% phenol degradation was achieved in 2 h.[17] The performance of phenol degradation on N-rGO-300 showed a significant improvement compared to rGO and 95% phenol degradation was achieved within 2 h on the N-rGO-300. Further improvement can be seen on N-rGO-325 and, 100% phenol degradation was observed in 1 h. Comparison of the activities of rGO, N-rGO-300 and N-rGO-325, it was suggested that SSA contributes less significantly than nitrogen doping to the enhanced performance of catalytic oxidation of phenol. The SSA values of N-rGO-300 (58 m^2/g) and N-rGO-325 (53 m^2/g) were lower than rGO (301 m^2/g). N-rGO-350, -375 and -400 had SSA values lower than unmodified rGO but showed very significant improvement in the performance of phenol degradation. Therefore, nitrogen doping might play the dominant role in phenol degradation on rGO-based catalysts. The doped nitrogen would change the electronic structure of carbon atoms nearby, and thus accelerate the electron transfer for the catalytic processes[17, 21]. The performance of N-rGO-350 was in good agreement with that of the previous study.[17] In this study, further annealing (two-step thermal annealing) of the N-rGO-350 at 400 °C in N_2 had very little effect on the improvement of the performance of phenol degradation. This result is consistent with those of the occurrence 2θ peaks, the SSA values, and the I_D/I_G ratios although decreasing B values or increasing L values. The effects of SSA and defective structure of rGO on the phenol degradation were not significant, evidenced by the fact that rGO with SSA of 301 m^2/g had a much lower activity than N-rGO-300 or -400 with SSAs of 53 – 153 m^2/g. Meanwhile, nitrogen doping would play a dominant role in activation of PMS for phenol oxidation, resulted in much higher phenol degradation efficiency. N-rGO-400 (SSA= 159 m^2/g) shows the best performance by reducing the phenol concentration from 100% to 0 within 15 min. Furthermore, no direct correlation between nitrogen dopants, including doping level and different nitrogen contents, and catalytic phenol oxidation was observed. This result suggests that, in terms of nitrogen doping, a relatively high SSA value may still contribute to the improved phenol degradation.

Further kinetic studies were carried out to investigate the effect of reaction temperature on phenol oxidation over N-rGO-350. Fig. S3 shows that phenol degradation almost follows linear correlation between Ln (phenol concentration) versus time, suggesting phenol degradation follows first order kinetics on N-rGO by activation of PMS. Fig. 8(b) shows that the activation energy was estimated to be 31.6 kJ/mol using the Arrhenius equation.

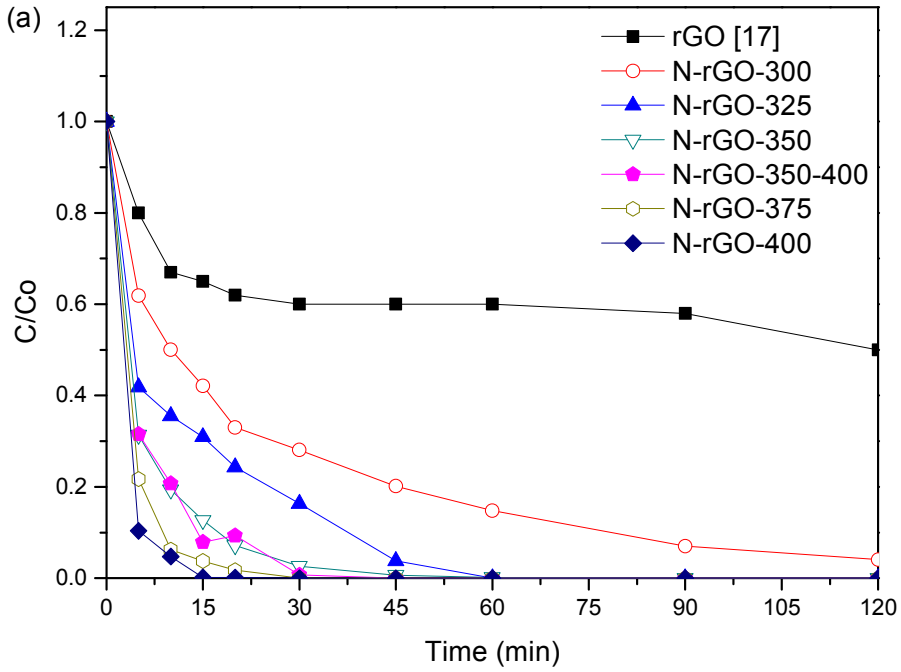

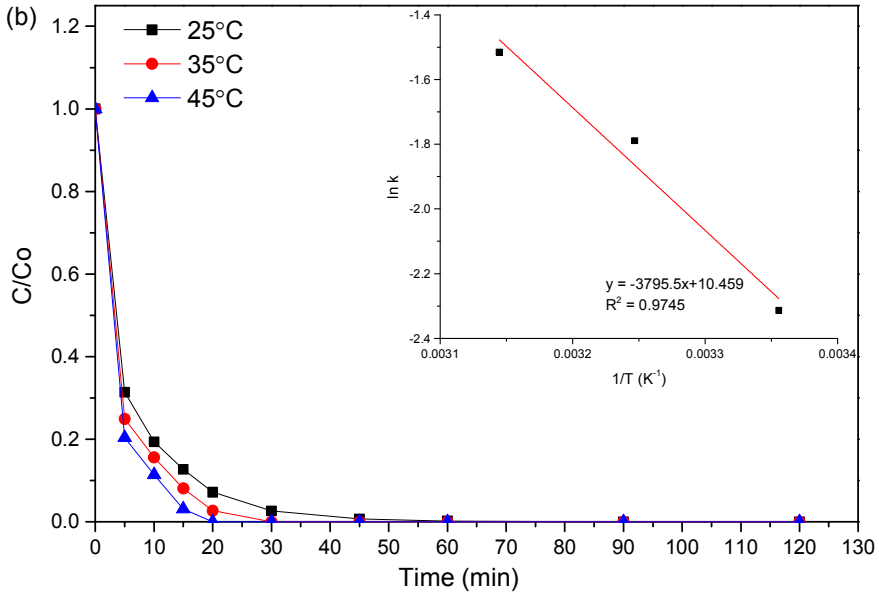

Figure 8 Catalytic degradation of phenol vs time on N-rGO at different thermal annealing temperatures by activation of PMS. (a) Phenol removal profiles on N-rGO, (b) Phenol removal profiles on N-rGO-350 at varying temperatures.

3.3 Mechanism of PMS activation and phenol oxidation

It was known that both $^{\bullet}OH$ and $SO_4^{\bullet-}$ radicals are generated during PMS activation by metal-based catalysts.[55, 56] $SO_4^{\bullet-}$ has been suggested to be the major radical for degradation of typical organic pollutants. In this study, rapid removal of phenol was obtained by PMS activation on N-rGO, especially on N-rGO-375 and N-rGO-400. In order to elucidate the mechanism of PMS activation on N-rGO for phenol degradation, electron paramagnetic resonance (EPR) studies were carried out, in which 5, 5-dimethyl-pyrroline-oxide (DMPO) was used as the spin trapping reagent for $^{\bullet}OH$ and $SO_4^{\bullet-}$ radicals.

Fig. 9 (a) shows the time-dependent radical generation at different reaction time (3, 5, 10, and 20 min). In all time, $^{\bullet}OH$ and $SO_4^{\bullet-}$ radicals were detected by EPR spectra. At 3 min, $^{\bullet}OH$ radicals occurred as the major species. This might indicate that $^{\bullet}OH$ radicals play a major role in catalytic phenol oxidation at initial stage.

It was known that $^{\bullet}OH$ and $SO_4^{\bullet-}$ radicals show different reaction rates with two radical scavengers, ethanol (EtOH) and tert-butyl alcohol (TBA) as the quenching agents.[56] EtOH can capture both $^{\bullet}OH$ and $SO_4^{\bullet-}$ while TBA prefers capturing $^{\bullet}OH$ radicals rather than $SO_4^{\bullet-}$ radicals. Figs. 9 (b) and (c) display the changes of reactive radicals generated by N-rGO activation of PMS with different quenching reagents. Both radicals and their changes upon addition of classical quenching reagents were identified.

Fig. 9 (d) shows the variation of the peak intensities of DMPO-HO and DMPO-SO_4 adducts during the reaction time (3, 5, 10 and 20 min) with and without the presence of the two scavengers, EtOH and TBA. It can be seen that, without scavengers, the DMPO-OH intensity increased significantly (N-rGO-350 DMPO-OH curve) within the reaction time of 3 min and decreased afterward (5-20 min). On the other hand, the DMPO-SO_4 intensity remained stable at a low level, which might be due to the great consumption of sulfate radicals in phenol oxidation. In the presence of EtOH, DMPO-OH intensity reduced and the peak occurred at 5 min. Meanwhile, in the presence of TBA, DMPO-OH intensity was much lower. However,

DMPO-SO_4 intensity did not show much difference with or without the scavengers. The above results suggest that both radicals are important in phenol degradation.

With the combination of EPR studies and classical quenching tests, it was confirmed that $^{\bullet}OH$ and $SO_4^{\bullet-}$ radicals are present in PMS activation for phenol oxidation on N-rGO catalysis. N-rGO would contribute to the electron transfer processes and facilitate below reactions.

$$HSO_5^- + e^- \rightarrow {}^{\bullet}OH + SO_4^{2-} \quad \text{Eq. (1)}$$

$$HSO_5^- + e^- \rightarrow SO_4^{\bullet-} + OH^- \quad \text{Eq. (2)}$$

$$HSO_5^- - e^- \rightarrow SO_5^{\bullet-} + H^+ \quad \text{Eq. (3)}$$

$$^{\bullet}OH + SO_4^{2-} \rightarrow SO_4^{\bullet-} + OH^- \quad \text{Eq. (4)}$$

$$SO_4^{\bullet-} + OH^- \rightarrow SO_4^{2-} + {}^{\bullet}OH \quad \text{Eq. (5)}$$

$$\text{Phenol} + SO_4^{\bullet-} (\ {}^{\bullet}OH\ ) \rightarrow \text{several steps} \rightarrow CO_2 + H_2O + SO_4^{2-} \quad \text{Eq. (6)}$$

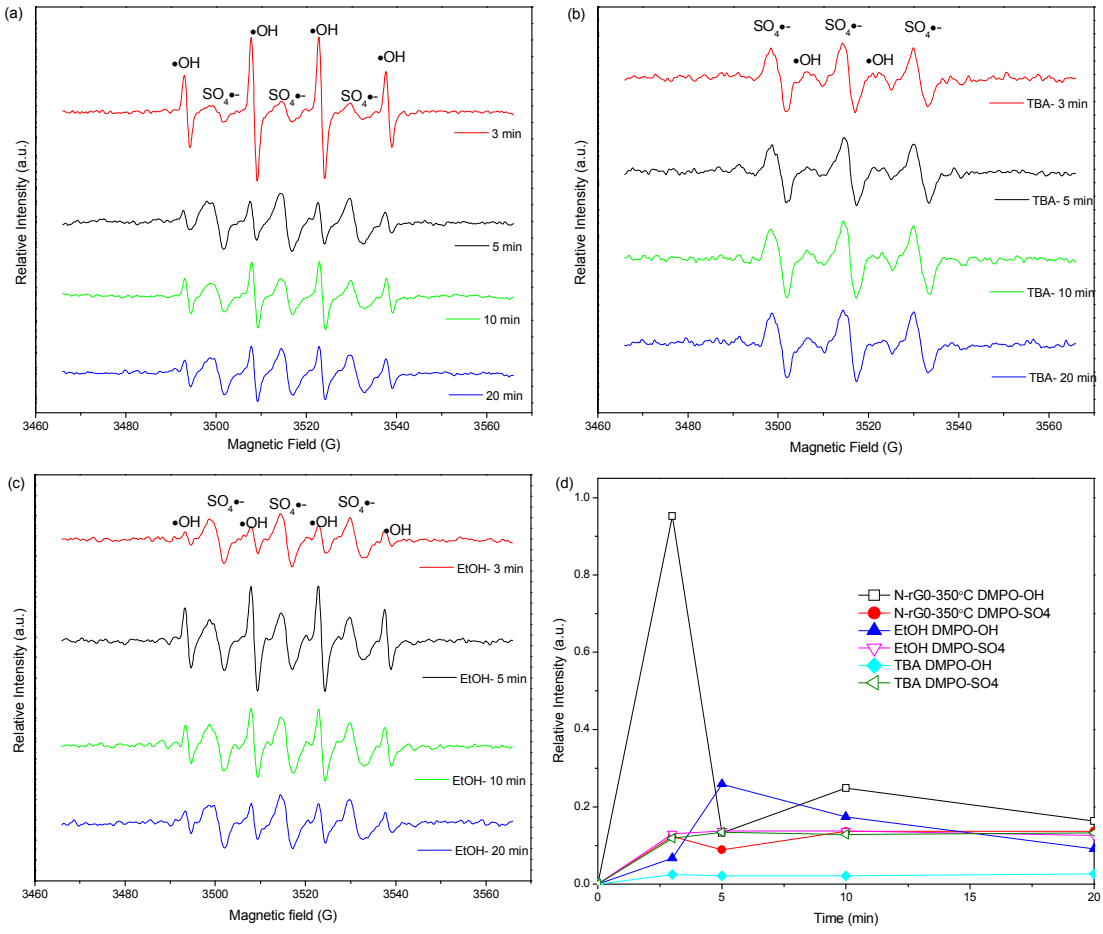

Figure 9 EPR spectra in various conditions, (a) PMS activation on N-rGO-350, (b) with addition of TBA, (c) with addition of EtOH, and (d) Comparison of hydroxyl and sulfate radicals dependence on time.

4. Conclusions

In this study, a simple method was used to successfully prepare nitrogen-doped reduced graphene oxide (N-rGO) by a simultaneous reduction and nitrogen doping of GO at low temperatures ranging from 300 to 400 °C. Comprehensive studies by a variety of characterization techniques suggested that significant crystal, structural and compositional modifications could be achieved by simply varying the calcination temperature for synthesis of highly efficient metal-free catalysts. These N-rGO materials as green catalysts were demonstrated to be efficient in catalytic activation of PMS for phenol degradation in water. For N-rGO via thermal annealing temperatures between 300 to 325 °C, the improvement of phenol degradation may be primarily due to the nitrogen dopant. Whereas for N-rGO from thermal annealing temperatures between 350 to 400 °C, the improvement of phenol degradation may be due to both nitrogen dopants and relatively high SSA. Combination of EPR studies and quenching tests indicated that N-rGO can activate PMS to produce both hydroxyl and sulfate radicals, which induce phenol degradation.

Acknowledgement

This work was financially supported by Australian Research Council (DP130101319). The authors acknowledge the use of equipment, scientific and technical assistance of the Curtin University Electron Microscope Facility which has been partially funded by the University, State and Commonwealth Governments. H. S. thanks the support from Curtin Research Fellowship.

Electronic Supplementary Information

Electronic supplementary information (ESI) available: XRD patterns, XPS spectra, and kinetic studies. See DOI: *******

References

1 H. W. Liang, Y. Y. Ting, H. Q. Sun, H. M. Ang, M. O. Tade and S. B. Wang, *J. Colloid Interface Sci.*, 2012, 372, 58-62.

2 P. Shukla, H. Q. Sun, S. B. Wang, H. M. Ang and M. O. Tade, *Sep. Purif. Technol.*, 2011, 77, 230-236.

3 P. R. Shukla, S. B. Wang, H. Q. Sun, H. M. Ang and M. Tade, *Appl. Catal., B*, 2010, 100, 529-534.

4 H. Q. Sun, H. W. Liang, G. L. Zhou and S. B. Wang, *J. Colloid Interface Sci.*, 2013, 394, 394-400.

5 E. Saputra, S. Muhammad, H. Q. Sun, H. M. Ang, M. O. Tade and S. B. Wang, *Appl. Catal., B*, 2014, 154, 246-251.

6 E. Saputra, S. Muhammad, H. Q. Sun, H. M. Ang, M. O. Tade and S. B. Wang, *Environ. Sci. Technol.*, 2013, 47, 5882-5887.

7 H. Q. Sun, G. L. Zhou, S. Z. Liu, H. M. Ang, M. O. Tade and S. B. Wang, *ACS Appl. Mater. Interfaces*, 2012, 4, 6235-6241.

8 H. W. Liang, H. Q. Sun, A. Patel, P. Shukla, Z. H. Zhu and S. B. Wang, *Appl. Catal., B*, 2012, 127, 330-335.

9 H. Q. Sun, S. Z. Liu, G. L. Zhou, H. M. Ang, M. O. Tade and S. B. Wang, *ACS Appl. Mater. Interfaces*, 2012, 4, 5466-5471.

10 W. C. Peng, S. Z. Liu, H. Q. Sun, Y. J. Yao, L. J. Zhi and S. B. Wang, *J. Mater. Chem. A*, 2013, 1, 5854-5859.

11 Y. J. Yao, S. D. Miao, S. Z. Liu, L. P. Ma, H. Q. Sun and S. B. Wang, *Chem. Eng. J.*, 2012, 184, 326-332.

12 S. Z. Liu, W. C. Peng, H. Q. Sun and S. B. Wang, *Nanoscale*, 2014, 6, 766-771.

13 S. B. Wang, H. Q. Sun, H. M. Ang and M. O. Tade, *Chem. Eng. J.*, 2013, 226, 336-347.

14 T. N. Huan, T. V. Khai, Y. Kang, K. B. Shim and H. Chung, *J. Mater. Chem.*, 2012, 22, 14756-14762.

15 R. Lv, Q. Li, A. R. Botello-Mendez, T. Hayashi, B. Wang, A. Berkdemir, Q. Z. Hao, A. L. Elias, R. Cruz-Silva, H. R. Gutierrez, Y. A. Kim, H. Muramatsu, J. Zhu, M. Endo, H. Terrones, J. C. Charlier, M. H. Pan and M. Terrones, *Sci. Rep.*, 2012, 2, 10.1038/srep00586.

16 J. Jiang, J. Turnbull, W. C. Lu, P. Boguslawski and J. Bernholc, *J. Chem. Phys.*, 2012, 136, 10.1063/1.3673441.

17 H. Q. Sun, Y. X. Wang, S. Z. Liu, L. Ge, L. Wang, Z. H. Zhu and S. B. Wang, *Chem. Commun.*, 2013, 49, 9914-9916.

18 S. Z. Liu, H. Q. Sun, S. M. Liu and S. B. Wang, *Chem. Eng. J.*, 2013, 214, 298-303.

19 L. T. Qu, Y. Liu, J. B. Baek and L. M. Dai, *ACS Nano*, 2010, 4, 1321-1326.

20 J. L. Long, X. Q. Xie, J. Xu, Q. Gu, L. M. Chen and X. X. Wang, *ACS Catal.*, 2012, 2, 622-631.

21 Y. J. Gao, G. Hu, J. Zhong, Z. J. Shi, Y. S. Zhu, D. S. Su, J. G. Wang, X. H. Bao and D. Ma, *Angew. Chem., Int. Ed.*, 2013, 52, 2109-2113.

22 H. Q. Sun, C. Kwan, A. Suvorova, H. M. Ang, M. O. Tade and S. B. Wang, *Appl. Catal., B*, 2014, 154, 134-141.

23 W. S. Hummers and R. E. Offeman, *J. Am. Chem. Soc.*, 1958, 80, 1339-1339.

24 S. D. Perera, R. G. Mariano, N. Nijem, Y. Chabal, J. P. Ferraris and K. J. Balkus, *J. Power Sour.*, 2012, 215, 1-10.

25 J. C. Charlier, X. Gonze and J. P. Michenaud, *Carbon*, 1994, 32, 289-299.

26 R. R. Haering, *Canad. J. Phys.*, 1958, 36, 352-362.

27 S. Park, J. An, J. R. Potts, A. Velamakanni, S. Murali and R. S. Ruoff, *Carbon*, 2011, 49, 3019-3023.

28 N. R. Wilson, P. A. Pandey, R. Beanland, J. P. Rourke, U. Lupo, G. Rowlands and R. A. Romer, *New J. Phys.*, 2010, 12, 21.

29 H. P. Klug and L. E. Alexander, *X-Ray Diffraction Procedures: For Polycrystalline and Amorphous Materials*, Wiley, 1974.

30 K. N. Kudin, B. Ozbas, H. C. Schniepp, R. K. Prud'homme, I. A. Aksay and R. Car, *Nano Lett.*, 2008, 8, 36-41.

31 D. Yang, A. Velamakanni, G. Bozoklu, S. Park, M. Stoller, R. D. Piner, S. Stankovich, I. Jung, D. A. Field, C. A. Ventrice and R. S. Ruoff, *Carbon*, 2009, 47, 145-152.

32 N. R. Wilson, P. A. Pandey, R. Beanland, R. J. Young, I. A. Kinloch, L. Gong, Z. Liu, K. Suenaga, J. P. Rourke, S. J. York and J. Sloan, *ACS Nano*, 2009, 3, 2547-2556.

33 W. Cai, R. D. Piner, F. J. Stadermann, S. Park, M. A. Shaibat, Y. Ishii, D. Yang, A. Velamakanni, S. J. An, M. Stoller, J. An, D. Chen and R. S. Ruoff, *Science*, 2008, 321, 1815-1817.

34 C. Gomez-Navarro, R. T. Weitz, A. M. Bittner, M. Scolari, A. Mews, M. Burghard and K. Kern, *Nano Lett.*, 2007, 7, 3499-3503.

35 M. J. McAllister, J. L. Li, D. H. Adamson, H. C. Schniepp, A. A. Abdala, J. Liu, M. Herrera-Alonso, D. L. Milius, R. Car, R. K. Prud'homme and I. A. Aksay, *Chem. Mater.*, 2007, 19, 4396-4404.

36 R. Bissessur, P. K. Y. Liu, W. White and S. F. Scully, *Langmuir*, 2006, 22, 1729-1734.

37 C. Xu, X. Wang, J. W. Zhu, X. J. Yang and L. Lu, *J. Mater. Chem.*, 2008, 18, 5625-5629.

38 M. Herrera-Alonso, A. A. Abdala, M. J. McAllister, I. A. Aksay and R. K. Prud'homme, *Langmuir*, 2007, 23, 10644-10649.

39 A. B. Bourlinos, D. Gournis, D. Petridis, T. Szabo, A. Szeri and I. Dekany, *Langmuir*, 2003, 19, 6050-6055.

40 Y. J. Yao, S. D. Miao, S. M. Yu, L. P. Ma, H. Q. Sun and S. B. Wang, *J. Colloid Interface Sci.*, 2012, 379, 20-26.

41 P. P. Guo, F. Xiao, Q. Liu, H. F. Liu, Y. L. Guo, J. R. Gong, S. Wang and Y. Q. Liu, *Sci. Rep.*, 2013, 3, 6, 10.1038/srep03499.

42 S. Boncel, S. W. Pattinson, V. Geiser, M. S. P. Shaffer and K. K. K. Koziol, *Beilstein J. Nanotechnol.*, 2014, 5, 219-233.

43 X. L. Li, H. L. Wang, J. T. Robinson, H. Sanchez, G. Diankov and H. J. Dai, *J. Am. Chem. Soc.*, 2009, 131, 15939-15944.

44 B. D. Guo, Q. A. Liu, E. D. Chen, H. W. Zhu, L. A. Fang and J. R. Gong, *Nano Lett.*, 2010, 10, 4975-4980.

45 L. F. Lai, J. R. Potts, D. Zhan, L. Wang, C. K. Poh, C. H. Tang, H. Gong, Z. X. Shen, L. Y. Jianyi and R. S. Ruoff, *Energ. Environ. Sci.*, 2012, 5, 7936-7942.

46 B. Zheng, J. Wang, F. B. Wang and X. H. Xia, *Electrochem. Commun.*, 2013, 28, 24-26.

47 Z. Q. Luo, S. H. Lim, Z. Q. Tian, J. Z. Shang, L. F. Lai, B. MacDonald, C. Fu, Z. X. Shen, T. Yu and J. Y. Lin, *J. Mater. Chem.*, 2011, 21, 8038-8044.

48 I. Y. Jeon, D. S. Yu, S. Y. Bae, H. J. Choi, D. W. Chang, L. M. Dai and J. B. Baek, *Chem. Mater.*, 2011, 23, 3987-3992.

49 D. H. Long, W. Li, L. C. Ling, J. Miyawaki, I. Mochida and S. H. Yoon, *Langmuir*, 2010, 26, 16096-16102.

50 S. Stankovich, D. A. Dikin, R. D. Piner, K. A. Kohlhaas, A. Kleinhammes, Y. Jia, Y. Wu, S. T. Nguyen and R. S. Ruoff, *Carbon*, 2007, 45, 1558-1565.

51 D. C. Wei, Y. Q. Liu, Y. Wang, H. L. Zhang, L. P. Huang and G. Yu, *Nano Lett.*, 2009, 9, 1752-1758.

52 S. Bag, K. Roy, C. S. Gopinath and C. R. Raj, *ACS Appl. Mater. Interfaces*, 2014, 6, 2691-2698.

53 G. Singh, D. S. Sutar, V. D. Botcha, P. K. Narayanam, S. S. Talwar, R. S. Srinivasa and S. S. Major, *Nanotechnology*, 2013, 24, 11.

54 X. J. Li, X. X. Yu, J. Y. Liu, X. D. Fan, K. Zhang, H. B. Cai, N. Pan and X. P. Wang, *Chin. J. Chem. Phys.*, 2012, 25, 325-329.

55. Z. F. Huang, H. W. Bao, Y. Y. Yao, W. Y. Lu and W. X. Chen, *Appl. Catal., B*, 2014, 154, 36-43.

56. Y. Wang, H. Sun, H. M. Ang, M. O. Tadé and S. Wang, *Appl. Catal., B*, 2015, 164, 159-167.